JGR Oceans

RESEARCH ARTICLE
10.1029/2020JC017080

Key Points:

- Ocean exchange flow at the 79 North Glacier exhibits considerable variability with standard deviations twice as large as the time mean flow
- Coherent, intra-seasonal fluctuations of the main ocean exchange flow across the calving fronts is enhanced in wintertime
- Intra-annual variability in the Atlantic water flow velocities at the glacier and upstream on the continental shelf co-vary at zero lag

Correspondence to:
L. von Albedyll,
luisa.von.albedyll@awi.de

Citation:
von Albedyll, L., Schaffer, J., & Kanzow, T. (2021). Ocean variability at Greenland's largest glacier tongue linked to continental shelf circulation. *Journal of Geophysical Research: Oceans*, *126*, e2020JC017080. https://doi.org/10.1029/2020JC017080

Received 14 DEC 2020
Accepted 23 APR 2021

Ocean Variability at Greenland's Largest Glacier Tongue Linked to Continental Shelf Circulation

Luisa von Albedyll[1], **Janin Schaffer**[1], **and Torsten Kanzow**[1,2]

[1]Helmholtz Centre for Polar and Marine Research, Alfred Wegener Institute, Bremerhaven, Germany, [2]University of Bremen, Bremen, Germany

Abstract Increased ocean-to-ice heat fluxes play a key role in the accelerated mass loss of Greenland's marine-terminating glaciers. Ocean current variability leads to variations in this heat flux. A year-long time series of ocean currents at all gateways to the ocean cavity under Greenland's largest remaining floating ice tongue at the Nioghalvfjerdsfjorden Glacier (79NG) was analyzed. The variability of the exchange flow at intra-annual to near-daily timescales was characterized. The currents exhibit considerable variability with standard deviations exceeding the time mean flow strength by a factor of 2. The inflow of warm Atlantic Intermediate Water into the cavity and the outflow via the northernmost calving front were directly coupled on intra-annual timescales (periods, $T > 30$ days) with enhanced fluctuations in the winter months. A strong correlation between the variability of the deep inflow and currents in the subsurface boundary current on the continental shelf suggests a link between cavity and continental shelf circulation. Variability on higher frequencies ($T < 30$ days) in the outflow was only partly induced by the inflow variability. Two export branches of the cavity circulation were identified, which were potentially constrained by subglacial meltwater channels. The relative importance of the two export branches varies on monthly time scales. This research has provided evidence that the large intra-annual ocean current variability at the 79NG is strongly influenced by the continental shelf circulation. Temporally varying preferred export routes increase the complexity of the cavity circulation.

Plain Language Summary The 79 North Glacier (79NG) in northeastern Greenland has the largest remaining floating ice tongue in Greenland. Like many others, the glacier tongue is melting, likely due to rising ocean temperatures. The amount of heat available for melting varies with the ocean temperatures and velocities supplying the cavity below the tongue with heat from the ocean. We wanted to better understand how and why the ocean speeds at the 79NG varied. Therefore, we deployed sensors that measured ocean velocities, temperature, and salinity next to the calving fronts between August 2016 and September 2017. We found that the ocean velocities varied strongly on timescales from several months to days. Comparing the variability at different gateways to the cavity revealed that more than half of the warm water flowing into the cavity is transported out via the calving front to the north. We showed that the variability in the inflow to the cavity is connected to the ocean currents transporting the warm water masses to the glacier from the continental shelf. This connection means that changes in the ocean currents several hundred kilometers away from the 79NG can have an impact on its melting.

1. Introduction

Accelerated mass loss from the Greenland Ice Sheet is responsible for 15% of the current rate of sea level rise, and climate models predict an increasing contribution by 2100 (Aschwanden et al., 2019; Marzeion et al., 2018). Increased ice discharge from outlet glaciers draining the Greenland Ice Sheet contributes 50% to the observed net mass loss; this dynamic loss is forced, to a large extent, by enhanced ocean-to-ice heat flux (e.g., Holland et al., 2008; IMBIE Team, 2020; Straneo & Heimbach, 2013; Straneo et al., 2013; van den Broeke et al., 2009).

The northeast Greenland Ice Stream drains about 12% of the Greenland Ice Sheet via three outlet glaciers: Nioghalvfjerdsbræ (79NG), Zachariæ Isstrøm, and Storstrømmen. Since the early 2000s, the northeast Greenland Ice Stream has lost mass (Figure 1a, Joughin et al., 2001; Mouginot et al., 2015; Khan et al., 2014). Ice discharge at Zachariæ Isstrøm increased by 50% between 1976 and 2015 due to enhanced oceanic heat fluxes and warmer air temperatures that led to the disintegration of the floating tongue (Mouginot et al., 2015;

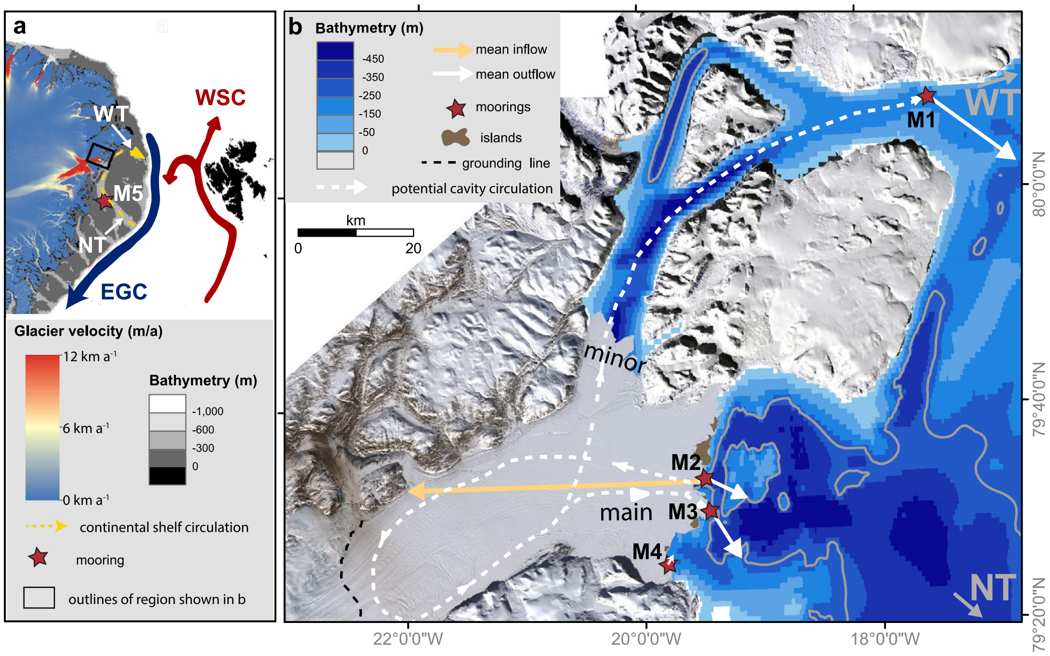

Figure 1. Cavity exchange flow across the calving fronts of the 79NG. (a) Northeast Greenland ice velocities (2017/2018) showing high speeds of the Northeast Greenland Ice Stream and the position of the 79 North Glacier (79NG). The main current system close to and on the northeast Greenland continental shelf are sketched, consisting of the West Spitsbergen Current (WSC)and its recirculating branch, the East Greenland Current (EGC), and the anti-cyclonic circulation of Atlantic Intermediate Water in Norske Trough (NT), monitored by mooring M5. The circulation expands to the north-east into Westwind Trough (WT). (b) The local bathymetry is displayed in blue. Stars mark the locations of the moorings M1–M4 at the 79NG main calving front and the mooring M1 in Dijmphna Sund in which the minor calving front ends. At each mooring site, the direction of the strongest ocean currents is indicated by a yellow arrow, indicating flow directed into the cavity or a white arrow, indicating flow directed out of the cavity. The current arrows are scaled by the maximum current speed (see Table 2). The white dashed lines draft a potential cavity circulation.

Schaffer et al., 2020). The ice tongue of the 79NG has been remarkably stable and is now the largest remaining ice tongue in Greenland (Figure 1b). However, Mayer et al. (2018) showed that the floating ice tongue of the 79NG has been out of mass balance equilibrium since 2001, resulting in a loss of 30% of its thickness between 1999 and 2014 (Mouginot et al., 2015; Wilson et al., 2017). Models predict a retreat of the grounding line of ~10 km within the next 80 years and further thinning of the floating ice tongue (Choi et al., 2017; Mayer et al., 2018). Since submarine melting accounts for 80% of the annual mass loss, excluding the rare calving events (Wilson et al., 2017), Mayer et al. (2018) speculated that increased ocean-to-ice heat flux has caused the thinning of the 79NG ice tongue.

The oceanic heat for the basal melting is provided by recirculating waters of Atlantic origin in Fram Strait that penetrate onto the northeast Greenland continental shelf; these waters are called Atlantic Intermediate Water (AIW; Bourke et al., 1987; Richter et al., 2018; Schaffer et al., 2017). Schaffer et al. (2017 and 2020) showed that the oceanic heat flux towards the 79NG increased since the late 1990s. A bottom-intensified boundary current transports the AIW through the trough system of Norske Trough from the southern shelf break to the 79NG (Figure 1a, Münchow et al., 2020; Schaffer et al., 2017). Within the ocean cavity under the ice tongue (hereafter called the "cavity") the AIW is cooled and freshened by basal melting and mixing with subglacial runoff, leaving the cavity as modified Atlantic Intermediate Water (mAIW) Schaffer et al. (2020) provides more details on the water mass properties.

Water mass transport across the calving fronts of the 79NG involves four distinct gateways shaped by the complex bathymetry (Schaffer et al., 2020, Figure 1b, see Table 1 for water depths). Three of the gateways are located at the large calving front that faces to the east (hereafter referred to as the *main calving front*). The fourth gateway is via the northern calving front that joins into Dijmphna Sund (Figure 1b, Mayer

Table 1
Overview of Moored Instruments Deployed at the Calving Fronts of the 79NG (M1-M4) and Close to Île de France (M5)

Mooring (water depth)	Position	Instrument (measured parameters)	Depth of measurements	Record length (mm/dd/yyyy)
M1 (172 m)	80° 8.92′N	ADCP 300 kHz (u,v)	168 m, bins: 164:4:60 m	08/29/2016 until 03/08/2017
	17° 24.56′ W	SBE 37 (T,C)	169 m	
M2 (474 m)	79° 34.13′N,	ADCP 150 kHz (p,u,v)	447 m, bins: 436:8:4 m	08/23/2016 until 09/23/2017
	19° 27.58′ W	SBE37 (p,T,C)	201 m	
		SBE56 (T)	227, 257, 287, 317,347, 377, 407, 427 m	
M3 (293 m)	79° 31.17′N	ADCP 75 kHz (p,u,v)	286 m, bins: 275:8:3 m	08/23/2016 until 09/23/2017
	19° 25.83′ W	SBE37 (p,T,C)	291 m	
M4 (326 m)	79° 26.40′N	ADCP 150 kHz (p,T,C)	320 m, bins 314:4:38 m	08/23/2016 until 09/21/2017
	19° 46.64′ W	SBE37 (p, T, C)	201 m	
		SBE56 (T)	236, 266, 296	
		SBE37 (T, C)	322 m	
M5 (416 m)	78° 09.02′N	ADCP 75 kHz	409 m, bins: 400:8:8 m	08/19/2016 until 09/29/2017
	15° 54.00′W			

Note. Measured parameters: u, eastward velocity; v, northward velocity; p, pressure; T, temperature; C, conductivity.

et al., 2000, hereafter referred to as the *minor calving front*). At the mouth of Dijmphna Sund a sill of 130 m depth blocks the exchange of Atlantic waters (Wilson & Straneo, 2015).

In addition to observed increased mean ocean-to-ice heat flux, there is observational evidence that the dynamics of marine-terminating glaciers are sensitive to sub-annual ocean forcing, for example, disintegration of the buttressing ice mélange or seasonal cycle in winds (e.g., Andersen et al., 2010; Gwyther et al., 2018; Howat et al., 2010; Pimentel et al., 2017). Sub-annual variability in ocean velocities and temperature can change glacier basal melt rates (Arzeno et al., 2014; Davis et al., 2018; Kirillov et al., 2017; Makinson et al., 2011). Jenkins et al. (2016) propose that variability in ocean conditions that is sufficiently large to force the grounding line off its stable position on a sill could trigger acceleration, thinning, and grounding line retreat, which may partly be non-reversible. Two recent studies identified considerable variability on time scales of days to several months in the ocean currents at the 79NG and subsequent significant variability in the heat flux to the glacier and basal melt rates (Lindeman et al., 2020; Schaffer et al., 2020). Thus, understanding the drivers and characteristics of this variability is crucial when assessing the ocean impact on the stability of the 79NG. To address this question, we require a detailed understanding of the exchange flow across the calving fronts and its variability.

Lindeman et al. (2020) suggested three potential mechanisms of ocean variability at the 79NG: (a) internal waves on the continental shelf that propagate into the cavity; (b) seasonal variability in subglacial runoff forcing that increases the export volume of mAIW in summer; and (c) variability of the hydraulically controlled inflow that links to changes in the outflowing mAIW with some lag. Schaffer et al. (2020) identified that oscillations in the AIW layer thickness at the sill separating the inflow to the cavity from the continental shelf circulation could alter the inflow strength. Remote drivers on the continental shelf may induce such oscillations. For example, Münchow et al. (2020) found that offshore Ekman pumping modulates the transport of AIW within the above mentioned bottom-intensified boundary current toward the inner shelf and the 79NG.

However, clear evidence for a link between the short-time ocean variability across the calving fronts and on the continental shelf is still missing. Furthermore, the variability of the ocean currents at the 79NG were so far only described considering two of the four exchange gateways to the glacier cavity (Lindeman et al., 2020). Since the large width of the main fjord allows for across-fjord variations in ocean current properties, an analysis of all four gateways would provide more detailed insights to the circulation (Figure 1b). This study presents ocean current and hydrographic observations from four moorings covering all exchange

Table 2
Mean Flow at Exchange gateways

	Mean flow magnitude (cm s^{-1})	Mean flow direction (°)	Strongest flow depth (m)	Strongest flow magnitude (cm s^{-1})	Transport (mSv)
M1	8.6 ± 15.0	131	144	12	19.7
M2 (inflow)	20.1 ± 16.3	266	436	38	43.7
M2	1.2 ± 5.5	117	164	3	8.5
M3	2.6 ± 6.0	146	179	5	11.2
M4	1.0 ± 5.0	9	126	2	4.3

Note. Flow magnitude is given as mean ± standard deviation and captures outflow unless specified otherwise. Flow direction is stated relative to the northward direction. For the strongest flow magnitude, the time-averaged flow in the depth bin of the strongest flow is given. For the balanced transport estimates see Section 2.1 and Schaffer et al. (2020). M2 (inflow) and M2 (outflow) comprise of the depths 243–436 m and 90–243 m, respectively.

gateways. We aim to characterize the temporal variability of the exchange flow across the calving fronts at near-daily to intra-annual timescales and link it to the continental shelf circulation.

2. Data and Methods

2.1. Moored Ocean Current Measurements

Moorings were deployed along the main calving front of the 79NG (M2, M3, and M4), in Dijmphna Sund (M1, Figure 1b), and in Norske Trough, close to Île de France (M5, Figure 1a) during the *Polarstern* cruise PS100 in August 2016 (Kanzow, 2017) and recovered during PS109 in September 2017 (Kanzow, 2018). Each mooring was equipped with a RDI Workhorse acoustic Doppler current profiler (ADCP) for ocean current measurements, temperature-salinity data loggers (SBE 37-SM/SMP MicroCAT manufactured by Sea-Bird Electronic) or temperature loggers (SBE 56 temperature loggers manufactured by Sea-Bird Electronics); see Table 1 for details of each mooring. The ADCPs recorded velocity in burst mode hourly/half-hourly with a minimal vertical resolution of 8 m. We quality-checked the data as described by Schaffer (2018) and linearly interpolated between the bin depths for every time step following Schaffer et al. (2020). Instruments at the main calving front (M2, M3, and M4) recorded data over the whole moored period; however, the ADCP in Dijmphna Sund (M1) stopped recording data on March 8, 2017.

Volume transports through each gateway were calculated following Schaffer et al. (2020). We find that the mean velocity profiles generally showed a decrease of velocities close to the seafloor. Therefore, we extrapolated the velocities from the deepest depth bin to the seafloor, presuming a further halving of the speed's amplitude at the bottom. We extrapolated the moored velocities horizontally to the sidewalls of the respective channel. To account for friction at the sidewalls, we reduced the velocities to 20% at horizontal distances of less than 500 m from the sidewalls while extrapolating horizontally. Vertically, we regridded the velocity fields to 5 m depth bins. The resulting velocity fields were multiplied at each depth bin with the respective width of the channel to estimate volume transports. The calculated mean residual mass transport across the calving fronts based on all moored measurements was close to zero. There was a deficit of −0.02 mSv (Sv = 1 Sverdrup = 10^6 m^3/s), that is, 0.04% of the total mean transport of 44 mSv (see Section 3.1, Table 2). We closed the mass budget at every time step individually by adding a time-varying, spatially uniform velocity to the velocity field, resulting into net compensated volume transports, that is, zero net flow across the calving fronts of the 79NG. For a detailed discussion on the uncertainties of the method, see Schaffer et al. (2020).

2.2. Time Series Analysis

We used common tools of time series analysis to describe the variability of the velocity data-set in time and space. Data gaps, accounting for about 0.02% of the data, were filled by linear interpolation. When applicable, we rotated the velocity fields into the direction of the strongest ocean velocities, and present the downstream component (see Figures 2–4, 6). To analyze the character of variability at different timescales,

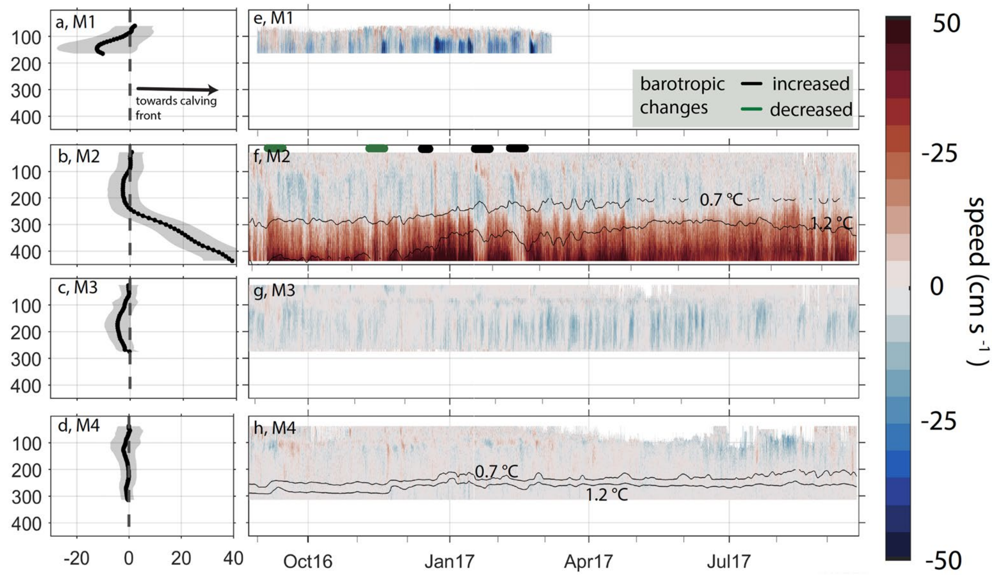

Figure 2. Rotated mean ocean velocities and time series at mooring M1–M4. (a–d) Mean ocean speed in the prevailing flow direction averaged for each depth (black dots) with the respective standard deviation (gray shading). (e–h) Ocean speed time series rotated into the prevailing flow direction, shown for each depth interval and the period from the end of August 2016 until September 2017. The depth of the 0.7°C and 1.2°C isotherm is overlaid in M2 and M4 as a black line. Barotropic events in the M2 record discussed in the text are marked as green and black lines.

we filtered the time series following a classification from von Appen et al. (2016). Period limits of 30, 2, and 0.25 days separated intra-annual variability (periods, $T > 30$ days) that reflects trend and seasonality, from a monthly component (2–30 days) that comprises mesoscale variability, including eddies. The near-daily range comprises periods between 0.25 and 2 days; a period range that is associated with semi-diurnal tides and inertial oscillations. We consider variability with periods smaller than 0.25 days to be high-frequency variability including noise and do not discuss them further. We constructed the filters using a Hanning filter (low-pass filter, cut-off period $T = 30$ days) and Butterworth filters of fourth-order with zero-phase (band-pass filters with cut-off periods of $T = 2$, $T = 0.25$ days) using the Matlab toolbox of J. Lilly (Lilly, 2017). We estimated tidal currents from the unfiltered velocity data using classical harmonic analysis as implemented in the Matlab routine T_Tide written by R. Pawlowicz, B. Beardsley, and S. Lentz (Pawlowicz et al., 2002).

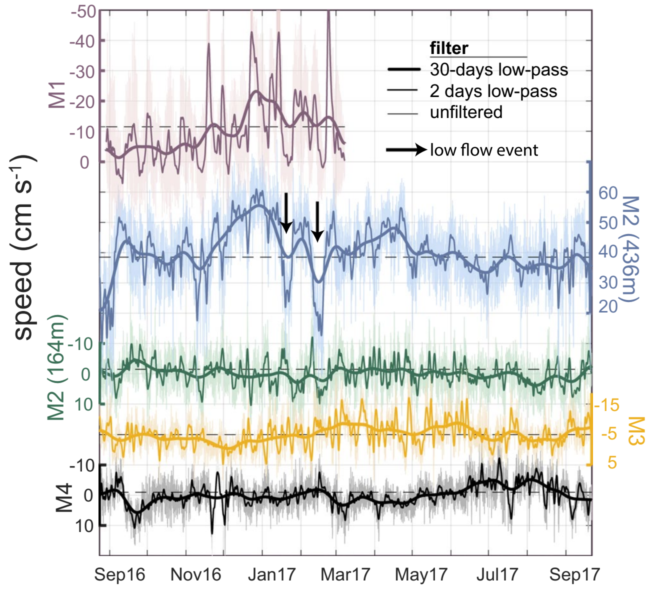

Figure 3. Filtered time series of ocean velocities rotated into the direction of the strongest flow at M1–M4. Each time series was filtered with a low-pass filter with a cut-off frequency of 30 days (thick dark line) and 2 days (thin dark line). The unfiltered velocity information is displayed as thin, light lines. For means of better comparisons with the inflow at M2 (436 m), the y-axes of the export gateways (M1, M2 (164 m), M3, and M4) were reversed. The black dashed line indicates the average velocity.

We regarded variability as the deviation from the mean flow and hence subtracted the mean before the calculations of the spectral estimates for each ocean current time series. We used the multi-taper method to reduce edge effects introduced by the Fourier transformation of a time series of finite length. We found that a set of eight Slepian tapers produced the best balance between a reduction of edge effects and blurring the signal. We chose a rotary spectrum that splits the velocity in a clockwise (positive) and counterclockwise (negative) sense of rotation of the circular components because it displayed more anisotropy than the Cartesian pairing. In preparation for the calculations, we combined the directional components of the velocity (u, v) into a complex number. The resulting spectral estimate of the rotary components were normalized such that the sum of the negative and the positive component approximated the variance of the time series. In this study, the variance was used as a measure of variability. We calculated variance per different frequency band by integrating the spectral estimate of the downstream component over the specified frequency range.

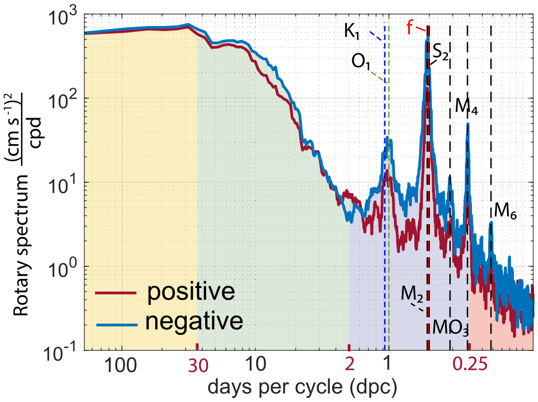

Figure 4. Rotary spectrum of the largest downstream component of ocean velocity at mooring M1. Tidal periods are displayed as dashed lines and labeled K_1, O_1, M_2, S_2, MO_3, M_4, and M_6. The Coriolis frequency f has a period of $T = 0.5080$ days per cycle. The spectrum was divided into four parts (intra-annual, monthly, near-daily, and high-frequency), that are shaded in different colors. The limits of the four parts are marked in red on the x-axis.

We constructed Empirical orthogonal functions (EOFs) from the compensated volume transports through the gateways from each depth bin. We confined the analysis to the time period in which data was available from all gateways (August 29, 2016 to March 08, 2017). EOFs decompose a signal Ψ into a linear combination of orthogonal functions ϕ (also called statistical "modes" scaled by a time-dependent amplitude $\alpha(t)$ (Talley et al., 2011). This can be written as:

$$\Psi(z_m, t) = \sum_{i=1}^{M} \alpha_i(t)\phi_i(m) \tag{1}$$

With the orthogonality condition (δ_{ij} is the Kronecker delta):

$$\sum_{m=1}^{M} \phi_i(m)\phi_j(m) = \delta_{ij} \tag{2}$$

where t is the time, m is the mode, and z_m the space coordinate. Before the calculations, we combined all transport records from the moorings M1, M2, M3, and M4 by concatenating the records along the vertical axis. Thus, z_m reflects not just a vertical, but a space coordinate, and we can identify variability shared among the different locations. This procedure resulted in 68 time series (thus $m = 68$) from the different sites and depths. Next, we filtered the volume transports into intra-annual, monthly, near-daily, and high-frequency contributions with the low-pass Hanning filter and band-pass Butterworth filters as described above. Then, we removed the time mean of the filtered time-series from the filtered time series at each location z_m, because we were most interested in the deviations from the mean flow that would otherwise dominate the strongest mode. We then carried out the EOF analysis on this pre-processed data set.

3. Results

In the following, we characterize the temporal variability of the exchange flow across the two calving fronts. First, we give an overview of the mean exchange flow (Section 3.1). Second, we analyze the temporal variability of the exchange flow at each gateway in different frequency bands (Section 3.2). Third, we identify spatial connections between the four exchange gateways (Section 3.3).

3.1. Mean Exchange Flow Across the Calving Fronts

The bathymetry at the 79NG allows flow exchange between the continental shelf and the cavity via four gateways (Section 1). Figures 1b and 2a–2d, and Table 2 illustrate and summarize the time-averaged flow profiles at those gateways rotated into the direction of the strongest ocean velocities.

The year-long measurements revealed that inflow of AIW took place exclusively through the deepest gateway at the center of the main calving front below 243 m (M2 inflow). Here, the mean flow with a magnitude of 20.1 cm s^{-1} was directed into the glacier cavity, that is, westward. The strongest inflow velocities were observed close to the bottom of the channel.

Mean outflow of mAIW, that is, eastward, took place at all four gateways below 90 m, which coincided with the average depth of the base of the main calving front. Strongest mean outflow velocities (8.6 cm s^{-1}) with less than half of the inflow speeds were recorded in Dijmphna Sund (M1) where the mean flow was directed towards the southeast (Table 2). The flow profile showed a bottom-intensified flow that was slowed down by bottom friction in the lowermost 20 m (Figure 2a). The large relative standard deviation of the mean flow (>200%) indicated significant variability of the flow, and is discussed in Section 3.2. Outflow velocities at M2 were only 14% of the speed at M1 and restricted to the upper layer between 90 and 243 m (Figure 2b,

Table 2). Further to the south, the time-averaged flow at M3 was directed towards the southeast. Low velocities close to the bottom at 293 m and the absence of water denser than a potential density of 1027.8 kg m^{-3} ruled out that this passage acts as a second gateway of AIW to the glacier cavity. The southernmost gateway (M4) was characterized by very low velocities (1.0 cm s^{-1}) directed towards the north-northeast. Even though the gateway may be deep enough to allow inflow and outflow, and temperature measurements indicated the presence of AIW below 207 m, the mooring recorded no significant exchange flow in the depth range below 240 m associated with mAIW. Consequently, we excluded this gateway as inflow to the cavity. Low velocities between 90 and 240 m indicated a minor export gateway for mAIW.

Balanced transport estimates (Section 2.1, Schaffer et al., 2020) were essentially consistent with the mean flow pattern and revealed a transport of 44 mSv into the cavity at the inflow depression (M2). Export at Dijmphna Sund accounted for almost half of the transport out of the cavity and outweighed all other export gateways (Table 2).

3.2. Temporal Variability of the Exchange Flow Across the Calving Fronts

Figures 2e–2h and 3 depict the ocean velocity time series at all depths and the depth of the strongest ocean velocity, respectively (Table 2). At M2 and M4, temperature loggers covering the water column provided sufficiently high vertical coverage (Table 1) to calculate the depth of the 0.7°C isotherm, which was used as an indicator for the interface between AIW and mAIW (Schaffer, 2017).

The time series of M1 (Figures 2f and 3) shows two periods with different distinct features. From September to mid-November, flow speeds alternated slightly around zero. From mid-November to March, we observed events of enhanced ocean velocities with up to 50 cm s^{-1} lasting for 5–10 days. Similarly, the ocean velocities time series of M2 (inflow) revealed an increase in velocities from December to January, followed by two fast drops in velocity of about 0.45 cm s^{-1} per hour. The current decelerated and the following low-flow period lasted for a total duration of 4–10 days (Figure 3). The time series of M2 (outflow), M3, and M4 bear only little resemblance with M1 and M2 (inflow, Figures 2 and 3). We did not find evidence for seasonal variability but observed that the flow varied on shorter, 1–2 days, timescales.

Both inflow and outflow at M2 varied considerably. Inflow velocities ranged between 0 and -70 cm s^{-1} and outflow velocities varied between -20 and 20 cm s^{-1}. Inflow and outflow at M2 experienced some common variability in the form of barotropic anomalies. They manifest themselves in (a) an increased outflow and decreased inflow, for example, end of December and end of January, when they shifted the reversing point of the flow in the vertical downwards by 100 m (black lines in Figure 2f), and (b) increased inflow at all depths; for example, mid-September and beginning of November (green lines in Figure 2f). During the yearlong observations the ocean velocity reversal point varied between 230 and 320 m. Interestingly, in 2016, the 0.7°C isotherm, defining the interface between mAIW and AIW, was located at the same depth where the flow reversed. From mid-November until January, the flow reversal point and the 0.7°C isotherm were lifted together, pointing to an increase in speed and thickness of the AIW layer. However, from the end of January onwards, the 0.7°C isotherm continued to rise (i.e., warming of the water) while the flow reversal point returned to a deeper level, resulting in an outward-directed flow of water masses with temperatures warmer than 0.7°C. In the one instrument measuring salinity at 201 m, we found a simultaneous increase in salinity and potential density from 34.48 ± 0.02 and 1027.66 ± 0.01 kg m^{-3} (August 23–November 15) to 34.55 ± 0.02 and 1027.71 ± 0.02 kg m^{-3} (February 1–September 21), respectively. Those observations suggest that both the AIW entering and the mAIW leaving the cavity warmed and became more saline.

Spectral estimates of the velocity at the depths of the strongest ocean velocities (Figure 3) of all five time series resembled each other strongly. The power density is largest at the lowermost frequencies and starts to decrease at a period of about 60 days. Only the near-daily band (periods of 0.25–2 days) is characterized by distinct peaks in power density, associated with tidal frequencies. As an example, Figure 4 shows the spectral estimate of the ocean velocities measurements at M1. The frequency bands of the timescales that are discussed below are shaded, and their variances are compared among the mooring records in Table 3. In the intra-annual frequency band, M2 (inflow) exhibited most variance compared to the other records (Table 3). Also, within the time series of M2 (inflow), the intra-annual frequency accounts for the largest part of the variance. Note that, due to the shorter duration of the time series recorded at Dijmphna Sund

Table 3
Relative Contributions of the Different Frequency Bands to the Total Variance of the Variability of the Downstream Component of the Flow (see Section 2.2)

	M1	M2 (inflow)	M2 (outflow)	M3	M4
intra-annual ($T > 30$ days)	15%	32%	10%	16%	24%
monthly (2–30 days)	30%	28%	31%	43%	31%
near-daily (0.25–2 days)	53%	20%	28%	31%	25%
high-frequency ($T < 0.25$ days)	4%	21%	32%	11%	21%
absolute variance	233 m^2s^{-2}	172 m^2s^{-2}	66 m^2s^{-2}	47 m^2s^{-2}	51 m^2s^{-2}

(M1), the variance of the intra-annual variability is not directly comparable to the other time series. The monthly frequency range (2–30 days) accounted for about a third of the total variance, strongly influencing the variability at all exchange gateways (Table 3). The near-daily range was dominated by distinct peaks at daily, semi-diurnal and quarter-diurnal frequencies (Figure 4). In Dijmphna Sund, half of the variance was present in this frequency band. We isolated tidal currents in the M1 time series. The semi-diurnal tide M_2 has a magnitude of 6.0 cm s^{-1} (semi-major axis), corresponding to 48% of the mean flow at the depth bin of the strongest ocean velocities (12.4 cm s^{-1}). The corresponding tidal ellipse was orientated parallel to the coastline (west-east). In the other gateways, 20%–31% of the variance was related to near-daily variability. The dominant frequencies correspond to the ones at M1, but they are more confined, that is, the energy is concentrated to a smaller frequency band. The tidal ellipses are orientated perpendicular to the main calving front, that is, mainly west-northwest to-east-southeast. High-frequency variability ($T < 0.25$ days) lacks clear-defined peaks. We note that it is much smaller at M1 than M2-M4, but refrain from discussing it further.

3.3. Spatial Variability of the Exchange Flow

Our analyses of the ocean velocity observations close to the 79NG calving fronts reveal a circulation system that consists of a single inflow of AIW at the center of the main calving front (M2 inflow) and the major outflow of mAIW through Dijmphna Sund (M1), complemented by outflow through the gateways at the main calving front (M2 outflow, M3, and M4). We further investigate spatially coherent variability to derive insights on cavity circulation patterns. At intra-annual timescales, inflow (M2) and outflow through Dijmphna Sund (M1) resembled each other (Figure 3). We specifically observed this behavior when current speeds at both sites simultaneously increased between November and March, followed by a joint strong current speed reduction that happened in the form of two synchronous events at the end of January and end of February, referred to as “low flow” events (Figure 3). They appeared first at M2 and with a delay of 3 and 24 h at M1, respectively. At shorter timescales, we could not find significant correlations between M1 and M2 (inflow). Normalized cross-covariance functions did not reveal any other significant correlation (with and without lag) between the ocean velocity time series of the other gateways.

We used EOFs to establish the spatial and temporal relationship between the transport through the different export gateways at intra-annual and monthly timescales. Applying filters before calculating the EOFs made patterns in the lower frequencies visible that were otherwise masked by the high variances associated with the tides and the high-frequency noise. The EOFs of the intra-annual variability illustrated that variability of the inflow was mainly mirrored by export through Dijmphna Sund (mode 1, 68% explained variance) and M2 (outflow, mode 2, 16% explained variance), meaning that inflow anomalies at one gate were often associated by outflow events at the other gate, and vice versa. In mode 1, enhanced inflow at M2 at depths exceeding 260 m was compensated by increased outflow at Dijmphna Sund and vice versa (Figure 5a). Mode 2 revealed baroclinic changes at M2, since the enhanced deep inflow was compensated by stronger, shallow outflow at M2 (100–270 m, Figure 5c). The principal component of mode 1 (PC1, Figure 5e) described the two main patterns of low (September–November) versus enhanced (November–March) outflow velocities at M1 (see Section 3.2). PC1 was negative from September until the end of November (reduced flow), and positive between end of November and March (increased flow). Most variance of the monthly variability was present in the upper water column, that is, the outflow, while the inflow remained almost constant

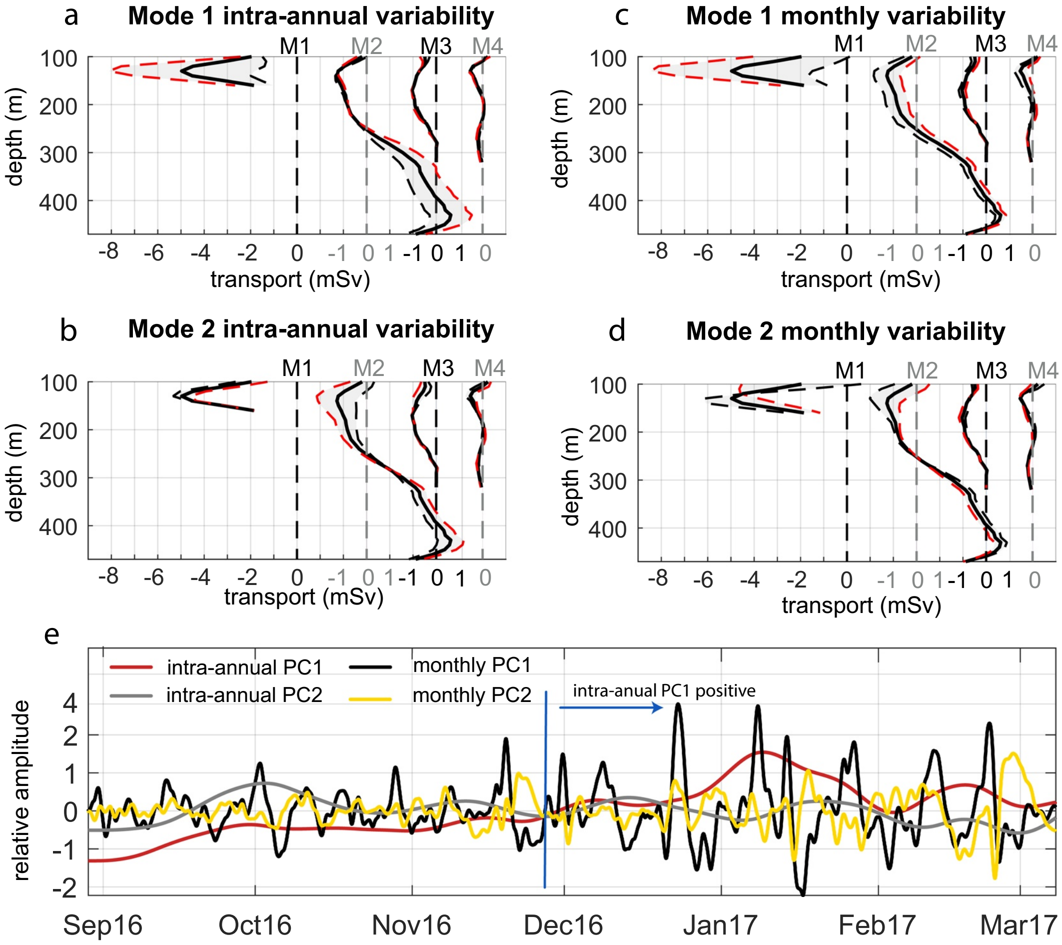

Figure 5. Empirical orthogonal functions (EOFs) of filtered time series. Panels (a–d) show mode 1 and 2 of the EOFs from the four gateways. Panels (a and b) show the EOFs based on 30 days low-pass filtered data (intra-annual) and (c and d) display the EOFs for 2–30 days band-pass filtered data (monthly variability). The thick black line indicates the mean flow at each mooring, and the modes are shown with dashed lines (red: positive, black: negative). (e), Time series of the two first principal components (PC1, PC2) of the modes shown in (a–d).

(Figure 5b). The first mode of the flow variability (48% explained variance) described a balance between the outflow through Dijmphna Sund and the outflow at the main calving front. The barotropic variability at the main calving front resulted in an increase of the inflow at depth at M2 synchronous with decreased outflow speeds at shallow depths at M2 and the two other gateways at the main calving front (M3, M4). Simultaneously, Dijmphna Sund reached its maximal export volume. The second mode of the monthly variability accounted for 16.8% (mode 3: 12%) and emphasized baroclinic changes in the upper 100–170 m at M1 that resulted into a reversal of the flow direction, that is, transport into Dijmphna Sund (Figure 5d). The principal components of both modes of the monthly variability had larger amplitudes from mid-December onwards (Figure 5e).

In summary, the EOFs of the intra-annual variability confirmed a strong link between deep inflow at M2 and outflow through Dijmphna Sund. The monthly variability revealed barotropic fluctuations at the main calving front that result in increased inflow and reduced outflow, which is balanced by enhanced outflow at the minor calving front through Dijmphna Sund.

3.4. Link Between Exchange Flow Across Calving Fronts and Continental Shelf Circulation

We investigated whether the continental shelf circulation is a potential driver of the variability observed at the calving front. Therefore, we compared the velocities of the inflow at the 79NG main calving front

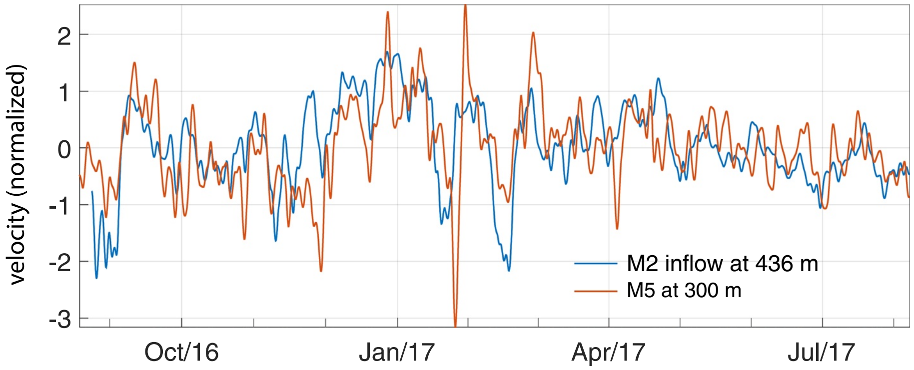

Figure 6. Normalized speed rotated in the direction of the strongest ocean velocities at M2 (main calving front) and M5 (Île de France). The time series are from the depth bin of the strongest ocean velocities (M2: 436 m, M5: 300 m). They have been normalized by their standard deviation and low-pass filtered (cut-off frequency 4 days). For details on the general current system and location of M5 see Figure 1.

(M2) and in the bottom-intensified boundary current transporting AIW towards the main calving front on the continental shelf (M5). The mooring M5 was located in Norske Trough close to Île de France, that is, southeast of the 79NG main calving front (Figure 6). At both locations, the depth bin with the strongest ocean velocities (M2: 436 m, M5: 300 m) was rotated into the main flow direction, detrended and normalized by its variance to visualize the variability that they have in common. If low-pass filtered at a cut-off period of 2 days, the velocity time series showed a significant correlation ($p < 0.05$) of $R = 0.48$. A low-pass filter of 30 days increased the correlation to $R = 0.61$. Filtering the signal with a band-pass filter of width 2 days and with variable start/endpoints from 1 to 60 days revealed that mainly the periods of 16–28 days and periods larger than 34 days contribute to the high correlation. The highest correlation was found for periods of 18 days. The coherent variability indicated that the intra-annual and the monthly variability with periods around 18 days of the exchange flow across the calving fronts were linked to the continental shelf circulation. In the following, we address relevant processes that may drive the observed variability pattern.

4. Discussion

The analysis of the ocean velocities from the calving fronts reveals different spatial patterns in the variability of the exchange flow across the calving fronts depending on the frequency band. We discuss potential drivers of the variability of each band and derive insights to the cavity circulation below.

4.1. Drivers of the Intra-Annual Variability

From the strong link at intra-annual timescales between the inflow at the main calving front and the outflow through Dijmphna Sund, we conclude that intra-annual variability is an essential part of the circulation below the glacier tongue. Ocean velocity observations from an ice-tethered mooring in the glacier tongue close to the minor calving front support this result. At that location, Lindeman et al. (2020) observed a major shift in the circulation pattern end of November, simultaneous to the increase in M2 inflow and M1 speeds observed in this study, indicated for example, by the sign change of the PC1 of the intra-annual variability (see Section 3.3, Figure 5). Schaffer et al. (2020) provided evidence that the inflow and its variability is controlled hydraulically by a sill in front of the inflow depression. They concluded that the density and height of the AIW layer upstream of the sill determines the volume flux and thus the strength of the circulation inside the cavity. These authors suggested that subglacial discharge at the grounding line has only a minor impact on driving the cavity circulation. Hence, the intra-annual variability of the exchange flow across the calving fronts is introduced by hydrographic variations upstream of the sill. In Section 3.4 we showed that those variations are not locally induced close to the sill, but propagate from the continental shelf to the glacier. The variability of the subsurface boundary current close to Île de France transporting AIW to the inner shelf (i.e., towards the 79NG) was recently analyzed by Münchow et al. (2020) for the years 2014–2016. They observed the strongest variability in the AIW transport in December and January and speculated that the variability of periods larger than 60 days was caused by seasonally variable sea-ice conditions and winds. They argued that winds and wind-stress curl peak during this time and that the sea ice is still sufficiently mobile, especially towards the continental shelf, to allow momentum-transfer between atmosphere and ocean. Even though the one-year-long time series from the 79NG presented in this study are too short to deduce a general winter enhancement of the intra-annual variability, the increased variability from November until March is consistent with the enhanced variability observed in winters 2014/2015 and 2015/2016 by Münchow et al. (2020) and in 1992/1993 by Topp and Johnson (1997). Since shelf winds were identified as drivers of winter-enhanced ocean currents across the continental shelves at other locations in Greenland (Fraser et al., 2018; Jackson et al., 2014), we highlight the need for future studies analyzing the relevance of shelf winds as drivers of the intra-annual variability by the means of multi-year ocean current time series.

In situ radar measurements have shown that basal melt rates under ice shelves may vary at daily to intra-annual timescales, correlated with the ocean heat content (Davis et al., 2018; Washam et al., 2019). Those observations are in contrast to a modeling study by Howat et al. (2010), who found that anomalies on timescales shorter than the residence time of waters in the cavity co-exist and balance each other in the spatial mean, resulting in a steady melt rate. Residence times of 162–380 days of the cavity overturning of the 79NG (Lindeman et al., 2020; Schaffer et al., 2020), point to adjustment timescales of the basal melting larger than most of the intra-annual variability. The extent to which sub-annual variability in the basal melt rate affects the long-term stability of the 79NG remains unclear. Several observational and modeling studies suggest that sub-annual variability in ocean velocities and temperature can increase glacier basal melt rates or trigger irreversible step changes (Arzeno et al., 2014; Davis et al., 2018; Kirillov et al., 2017; Makinson et al., 2011). Modeling studies of glacier melt should therefore include both long-term climate variability and short-term forcing.

Lindeman et al. (2020) discussed seasonal subglacial discharge as a source for the low variability of ocean velocities at M4. Since we could not identify a seasonal cycle in the time series of M1, M2, and M3, we assume that, at those locations, the weaker runoff signal is most likely obscured by variability induced by the continental-shelf circulation.

We cannot exclude the possibility that longer (inter-annual) variability is also present in the time series but cannot be distinguished from the intra-annual variability. Considering the long-term thickening (Schaffer et al., 2020) and warming (Schaffer et al., 2017) of the AIW layer observed since the late 1990s, we would require a time series of multiple years to differentiate the long-term trend from the intra-annual variability.

4.2. Monthly Variability Related to the Cavity Circulation

On monthly timescales, we find a balance between barotropic variability at the main calving front and the export through the minor calving front in Dijmphna Sund. We propose two sources of this variability, (1) originating from the continental shelf and (2) originating from within the cavity. The flow in the subsurface boundary current transporting AIW to the 79NG and the inflow across the front exhibits coherent motion at periods of about 18 days. Münchow et al. (2020) identified at the same location very similar variability with periods of about 20 days in 2014–2016. They attributed the ocean velocity variability to energetic topographic Rossby waves that propagate along the inflow gateway of AIW from the shelf edge toward the 79NG. The waves are likely to be generated by time variable Ekman pumping over the shelf break that shows enhanced variability in winter. We find the largest correlation between M5 and M2 at periods at 18 days, close to the 20 days periods in Münchow et al. (2020). In addition, we observe a winter enhancement. This agreement with Münchow et al. (2020) hint at a similar forcing mechanism for this part of the monthly variability in 2016–2017. Those results are in line with Lindeman et al. (2020), who found evidence for fast changes in T-S characteristics associated with isopycnal oscillations induced by such waves.

The export of mAIW at the main calving front of the 79NG is distributed over three gateways (see Table 2). We speculate that spatially varying export through the three gateways induces monthly variability. The EOFs of the monthly variability indicate that the export across the calving fronts is alternating between outflow through Dijmphna Sund and the main calving front. We observe that the export of mAIW by the cavity circulation is split into two main branches with nearly equal contributions of 46% export via Dijmphna Sund and 54% via the main calving front. The relative importance of the two branches seems to vary on monthly timescales. The branch of Dijmphna Sund appears more strongly linked to the inflow than the main calving front because the dominant variability of the inflow (intra-annual) is found synchronized at M1 and M2. Considering that rotation (i.e., Coriolis force) should play a role because the cavity width is wider (Mayer et al., 2000) than the baroclinic Rossby radius (about 14 km in this region, Münchow et al., 2020), the outflow of mAIW from the grounding line should be deflected to the southern part of the cavity. Therefore, Dijmphna Sund should be less prone to serve as major outflow gateway. Those considerations contradict the observations and lead us to assume that spatially differing ice bottom topography of the glacier tongue at the grounding line could provide strong guidance to the flow, as suggested by for example, Millgate et al. (2013). A transverse profile along the ice base retrieved from the assumption of hydrostatic equilibrium of the ice tongue shows the presence of two pronounced subglacial meltwater channels at the center and the southern flank of the glacier (Wilson et al., 2017). The strongly spatially varying melt rates across the glacier tongue towards the calving fronts indicate the continuation of those channels towards the calving fronts (Wilson et al., 2017). Subglacial run-off at the grounding line enhances the turbulent ocean heat and salt flux to the shelf-ocean interface increasing local melting. The channels potentially reinforce their geometry by experiencing faster velocities due to convergence of less dense water in their center and hence more substantial melt (Millgate et al., 2013; Rignot & Steffen, 2008). However, it remains unclear which processes related to the subglacial channels could induce the observed temporal variability. The location of the subglacial channels depends on transverse differences in ice thickness and varies most likely on longer timescales related to the glacier speed of about 12 km a^{-1} (Dallaston et al., 2015; Wilson et al., 2017). Varying subglacial discharge could reduce the variability during the winter months. Since we cannot distinguish between monthly variability introduced by the inflow enhanced in winter and variability only present in the outflow, we are not able to confirm this connection.

We argue that the strong link between inflow across the main calving front and outflow through Dijmphna Sund points to a concentrated, topographically steered flow towards the north. From the lack of coherence of the time series at M2, M3, and M4 we hypothesize that the branch towards the main calving front appears less focused, potentially experiencing more disturbance while splitting into the three different outflows. Similarly, Lindeman et al. (2020) identified a complicated, temporally changing circulation pattern below the glacier tongue that exhibited phases of primarily horizontally sheared exchange flows. Their slightly different conclusions on the gateway of the main outflow based on the observations at the northern flank of the glacier tongue highlights the spatial inhomogeneity and complexity of the circulation.

Spatial variability of the outflow may also be introduced by the complex bathymetry at the main calving front. The interaction of meltwater plumes with the islands present at the main calving front may cause a more diffuse, three-dimensional outflow signal with multiple meltwater plumes interacting. At the fjord mouth of Dijmphna Sund, at a distance to the minor calving front, the lateral gradients may have been reduced by mixing, thus resulting in a more two-layer circulation (Straneo & Cenedese, 2015) relative to the outflows through the gateways at the main calving front. This could contribute to the larger agreement between inflow at depth (M2 inflow) and outflow in Dijmphna Sund (M1).

4.3. Near-Daily Variability Induced by Tides

Variability on near-daily timescales is mainly caused by tides (Figure 4). The magnitude of the observed tidal currents of 6 cm s^{-1} in Dijmphna Sund matches well with the findings of Topp and Johnson (1997) that described an M_2 component of 3–5 cm s^{-1} in Westwind Trough, but are 2.5 times larger than the speeds observed by Lindeman et al. (2020) below the glacier tongue. Compared to the wide main calving front, more than narrow fjord geometry and the shallow water depths in Dijmphna Sund might have enhanced the tidal currents. Below floating ice tongues sheltered from winds, tides have been identified as an important source of kinetic energy for conversion to vertical mixing (e.g., Mueller et al., 2012). Arzeno et al. (2014) estimated that tides cause an increase in the basal melt rates by 50%, for a zone near the front of the Ross Ice Shelf, Antarctica. A study from Flade Isblink (northeast Greenland) has demonstrated that tidal velocities low as 1–2 cm s^{-1} may already contribute to water renewal at the calving front in the absence of a strong mean flow and induce internal waves Kirillov et al. (2017). However, compared to the strong inflow speeds of 20.1 cm s^{-1} (Table 2) we propose that tides make only a minor contribution to melt rates at the 79NG.

5. Conclusion

Sub-annual ocean current variability close to marine-terminating glaciers modulates ocean-to-ice heat flux, potentially changing glacier dynamics. We have used data from several moorings in 2016–2017 to characterize the temporal variability of the exchange flow across the calving fronts of the 79NG, and identify links to the continental shelf circulation. Analyzing ocean velocity observations from all gateways to the cavity of the 79NG, covering a period of 7–12 months, reveals an exchange flow that comprises a single inflow at the center of the main calving front and two equally important outflow branches. The export of glacially mAIW takes place at the minor calving front through Dijmphna Sund and along the main calving front through three exchange gateways. The ocean velocities are characterized by considerable variability on intra-annual to near-daily timescales, that revealed spatial links between the branches and the continental shelf circulation.

On intra-annual timescales (periods, $T > 30$ days), the outflow branch via Dijmphna Sund appears directly linked to the deep inflow, while the branch to the main calving front exhibits a more complicated flow. The coherent intra-annual variability of Dijmphna Sund outflow and the deep inflow is enhanced in the winter months between November 2016 and March 2017. We showed that the variability of the inflow is also present 170 km south of the main calving front in the subsurface boundary current transporting the warm AIW to the 79NG. We conclude that the exchange flow across the calving fronts is strongly linked to the large-scale continental shelf circulation on intra-annual timescales. Considering the large variations in ocean heat flux to the glacier base, we speculate that the intra-annual variability may introduce sub-annual variability in the basal melt rates (see also Lindeman et al., 2020; Schaffer et al., 2020). The monthly variability (2–30 days) accounts for about one third of the total variance of the time series. Since variability with periods of about 18 days in the inflow correlate strongly with the ocean velocities in the subsurface boundary current, we speculate that a large-scale driver, for example, topographic Rossby waves introduced by Ekman pumping over the shelf break (Münchow et al., 2020) are responsible for this variability. Furthermore, empirical orthogonal functions revealed that a part of the monthly variability is uncoupled from the variability in the deep inflow. We cannot exclude the possibility that temporarily varying export through different meltwater channels at the grounding line also induced monthly variability.

Tidal currents are the main forcing of the near-daily variability (0.25–2 days) that is most pronounced at Dijmphna Sund where they account for half of the variance. Our description of the ocean velocity variability of the exchange flow across the calving fronts of the 79NG raises to the likelihood that large magnitudes of sub-annual variability might be occurring in other glacial fjords in Greenland and have significant implications for ice loss in those other systems. Our results suggest links between variability of currents and heat fluxes at the glacier mouth and oceanographic currents and hydrographic properties on the continental shelf. We conclude that, for understanding ocean-glacier interaction, the whole temporal and spatial range of oceanic variability in heat transport needs to be taken into account, including intra-seasonal and shorter timescales.

Data Availability Statement

Raw mooring data are available at the World Data Center PANGAEA under https://doi.pangaea.de/10.1594/PANGAEA.904023. Processed mooring data are found under https://doi.pangaea.de/10.1594/PANGAEA.909471 together with a report on data processing (Schaffer, 2018). Satellite images recorded by Landsat 8 on April 28, 2016 (Figure 1b) can be downloaded from Earth Explorer (https://earthexplorer.usgs.gov/) courtesy of the US Geological Survey. Ice velocities based on Greenland ice velocity map 2017/2018 from Sentinel-1 [version 1.0] and the grounding-line position derived from ERS-1/-2 SAR and Sentinel-1 SAR interferometry displayed in Figure 1 are available from ENVEO within the ESA Initiative Greenland Ice Sheet CCI (http://esa-icesheets-greenland-cci.org/). The interpolated bathymetry grid for northeast Greenland with a 250 m grid resolution that includes multibeam echo-sounding data collected in 2016 in front of 79NG are available at https://doi.pangaea.de/10.1594/PANGAEA.909628.

Acknowledgments

The authors thank Rebecca McPherson for her valuable feedback on copy editing. We acknowledge the contribution of all crew and participants onboard R/V Polarstern during PS100 and PS109 and support from the German Federal Ministry for Education and Research (BMBF) within the GROCE project (Grant 03F0778A). Ship time was provided under Grants AWI_PS100_01 and AWI_PS109_03. The authors thank two anonymous reviewers for their comments and suggestions that significantly improved both clarity and precision of the study.

References

Andersen, M. L., Larsen, T. B., Nettles, M., Elosegui, P., van As, D., Hamilton, G. S., et al (2010). Spatial and temporal melt variability at Helheim glacier, East Greenland, and its effect on ice dynamics. *Journal of Geophysical Research*, *115*(F4). https://doi.org/10.1029/2010jf001760

Arzeno, I. B., Beardsley, R. C., Limeburner, R., Owens, B., Padman, L., Springer, S. R., et al. (2014). Ocean variability contributing to basal melt rate near the ice front of Ross Ice Shelf, Antarctica. *Journal of Geophysical Research: Oceans*, *119*(7), 4214–4233. https://doi.org/10.1002/2014jc009792

Aschwanden, A., Fahnestock, M. A., Truffer, M., Brinkerhoff, D. J., Hock, R., Khroulev, C., & Khan, S. A. (2019). Contribution of the Greenland ice sheet to sea level over the next Millennium. *Science Advances*, *5*, eaav9396.

Bourke, R. H., Newton, J. L., Paquette, R. G., & Tunnicliffe, M. D. (1987). Circulation and water masses of the East Greenland shelf. *Journal of Geophysical Research*, *92*(C7), 6729–6740. https://doi.org/10.1029/jc092ic07p06729

Choi, Y., Morlighem, M., Rignot, E., Mouginot, J., & Wood, M. (2017). Modeling the response of Nioghalvfjerdsfjorden and Zachariae Isstrøm glaciers, Greenland, to ocean forcing over the next century. *Geophysical Research Letters*, *44*(21), 11071−11079. https://doi.org/10.1002/2017gl075174

Dallaston, M. C., Hewitt, I. J., & Wells, A. J. (2015). Channelization of plumes beneath ice shelves. *Journal of Fluid Mechanics*, *785*, 109–134. https://doi.org/10.1017/jfm.2015.609

Davis, P. E. D., Jenkins, A., Nicholls, K. W., Brennan, P. V., Abrahamsen, E. P., Heywood, K. J., et al (2018). Variability in basal melting beneath pine island ice shelf on weekly to monthly timescales. *Journal of Geophysical Research: Oceans*, *123*(11), 8655–8669. https://doi.org/10.1029/2018jc014464

Fraser, N. J., Inall, M. E., Magaldi, M. G., Haine, T. W. N., & Jones, S. C. (2018). Wintertime Fjord-Shelf interaction and ice sheet melting in Southeast Greenland. *Journal of Geophysical Research: Oceans*, *123*(12), 9156–9177. https://doi.org/10.1029/2018jc014435

Gwyther, D. E., O'Kane, T. J., Galton-Fenzi, B. K., Monselesan, D. P., & Greenbaum, J. S. (2018). Intrinsic processes drive variability in basal melting of the Totten glacier ice shelf. *Nature Communications*, *9*(1). https://doi.org/10.1038/s41467-018-05618-2

Holland, D. M., Thomas, R. H., de Young, B., Ribergaard, M. H., & Lyberth, B. (2008). Acceleration of Jakobshavn Isbræ triggered by warm subsurface ocean waters. *Nature Geoscience*, *1*(10), 659–664. https://doi.org/10.1038/ngeo316

Howat, I. M., Box, J. E., Ahn, Y., Herrington, A., & McFadden, E. M. (2010). Seasonal variability in the dynamics of marine-terminating outlet glaciers in Greenland. *Journal of Glaciology*, *56*(198), 601–613. https://doi.org/10.3189/002214310793146232

IMBIE Team. (2020). Mass balance of the Greenland ice sheet from 1992 to 2018. *Nature*, *579*(7798), 233–239. https://doi.org/10.1038/s41586-019-1855-2

Jackson, R. H., Straneo, F., & Sutherland, D. A. (2014). Externally forced fluctuations in ocean temperature at Greenland glaciers in non-summer months. *Nature Geoscience*, *7*(7), 503–508. https://doi.org/10.1038/ngeo2186

Jenkins, A., Dutrieux, P., Dutrieux, P., Jacobs, S., Steig, E., Gudmundsson, H., et al. (2016). Decadal ocean forcing and Antarctic ice sheet response: Lessons from the Amundsen sea. *Oceanography*, *29*(4), 106–117. https://doi.org/10.5670/oceanog.2016.103

Joughin, I., Fahnestock, M., MacAyeal, D., Bamber, J. L., & Gogineni, P. (2001). Observation and analysis of ice flow in the largest Greenland ice stream. *Journal of Geophysical Research*, *106*(D24), 34021–34034. https://doi.org/10.1029/2001jd900087

Kanzow, T. (2017). The expedition PS100 of the Research Vessel POLARSTERN to the Fram Strait in 2016. *Reports on Polar and Marine Research*. *705*. https://doi.org/10.2312/bzpm_0705_2017

Kanzow, T. (2018). The expedition PS109 of the Research Vessel POLARSTERN to the Nordic Seas in 2017. *Reports on Polar and Marine Research*. *715*. https://doi.org/10.2312/BzPM07152018

Khan, S. A., Kjær, K. H., Bevis, M., Bamber, J. L., Wahr, J., Kjeldsen, K. K., et al (2014). Sustained mass loss of the northeast Greenland ice sheet triggered by regional warming. *Nature Climate Change*, *4*(4), 292–299. https://doi.org/10.1038/nclimate2161

Kirillov, S., Dmitrenko, I., Rysgaard, S., Babb, D., Toudal Pedersen, L., Ehn, J., et al. (2017). Storm-induced water dynamics and thermohaline structure at the tidewater Flade Isblink Glacier outlet to the Wandel Sea (NE Greenland). *Ocean Science*, *13*(6), 947–959. https://doi.org/10.5194/os-13-947-2017

Lilly, J. M. (2017). jLab: A data analysis package for Matlab (Tech. Rep.). Retrieved from http://www.jmlilly.net/jmlsoft.html

Lindeman, M. R., Straneo, F., Wilson, N. J., Toole, J. M., Krishfield, R. A., Beaird, N. L., et al. (2020). Ocean circulation and variability beneath Nioghalvfjerdsbræ (79 North Glacier) ice iongue. *Journal of Geophysical Research: Oceans*, *125*(8), e2020JC016091. https://doi.org/10.1029/2020jc016091

Makinson, K., Holland, P. R., Jenkins, A., Nicholls, K. W., & Holland, D. M. (2011). Influence of tides on melting and freezing beneath Filchner-Ronne Ice Shelf, Antarctica. *Geophysical Research Letters*, *38*(6), L06601. https://doi.org/10.1029/2010gl046462

Marzeion, B., Kaser, G., Maussion, F., & Champollion, N. (2018). Limited influence of climate change mitigation on short-term glacier mass loss. *Nature Climate Change*, *8*(4), 305–308. https://doi.org/10.1038/s41558-018-0093-1

Mayer, C., Reeh, N., Jung-Rothenhäusler, F., Huybrechts, P., & Oerter, H. (2000). The subglacial cavity and implied dynamics under Nioghalvfjerdsfjorden glacier, NE-Greenland. *Geophysical Research Letters*, *27*(15), 2289–2292. https://doi.org/10.1029/2000gl011514

Mayer, C., Schaffer, J., Hattermann, T., Floricioiu, D., Krieger, L., Dodd, P. A., et al. (2018). Large ice loss variability at Nioghalvfjerdsfjorden glacier, Northeast-Greenland. *Nature Communications*, *9*(1). https://doi.org/10.1038/s41467-018-05180-x

Millgate, T., Holland, P. R., Jenkins, A., & Johnson, H. L. (2013). The effect of basal channels on oceanic ice-shelf melting. *Journal of Geophysical Research: Oceans*, *118*(12), 6951–6964. https://doi.org/10.1002/2013jc009402

Mouginot, J., Rignot, E., Scheuchl, B., Fenty, I., Khazendar, A., Morlighem, M., et al (2015). Fast retreat of Zachariae Isstrom, northeast Greenland. *Science*, *350*(6266), 1357–1361. https://doi.org/10.1126/science.aac7111

Mueller, R. D., Padman, L., Dinniman, M. S., Erofeeva, S. Y., Fricker, H. A., & King, M. A. (2012). Impact of tide-topography interactions on basal melting of Larsen C Ice Shelf, Antarctica. *Journal of Geophysical Research*, *117*(C5), C05005. https://doi.org/10.1029/2011jc007263

Münchow, A., Schaffer, J., & Kanzow, T. (2020). Ocean circulation connecting Fram Strait to glaciers off northeast Greenland: Mean flows, topographic Rossby waves, and their Forcing. *Journal of Physical Oceanography*, *50*, 509–530. https://doi.org/10.1175/JPO-D-19-0085.1

Pawlowicz, R., Beardsley, B., & Lentz, S. (2002). Classical tidal harmonic analysis including error estimates in MATLAB using T_TIDE. *Computers & Geosciences*, *28*(8), 929–937. https://doi.org/10.1016/s0098-3004(02)00013-4

Pimentel, S., Flowers, G. E., Sharp, M. J., Danielson, B., Copland, L., Van Wychen, W., et al (2017). Modeling intra-annual dynamics of a major marine-terminating arctic glacier. *Annals of Glaciology*, *58*(74), 118–130. https://doi.org/10.1017/aog.2017.23

Richter, M. E., von Appen, W.-J., & Wekerle, C. (2018). Does the East Greenland current exist in the northern Fram Strait? *Ocean Science*, *14*(5), 1147–1165. https://doi.org/10.5194/os-14-1147-2018

Rignot, E., & Steffen, K. (2008). Channelized bottom melting and stability of floating ice shelves. *Geophysical Research Letters*, *35*(2). https://doi.org/10.1029/2007gl031765

Schaffer, J. (2017). *Ocean impact on the 79 North Glacier, Northeast Greenland*(Doctoral dissertation).University of Bremen. Retrieved from https://elib.suub.uni-bremen.de/peid=D00106281

Schaffer, J. (2018). *Report on mooring processing of ps109/ps114 recoveries (ne greenland continental shelf)*. Retrieved from hdl:10013/epic.4cf66b0e-b6c2-4e0c-aef1-a709c493c1dc

Schaffer, J., Kanzow, T., von Appen, W.-J., von Albedyll, L., Arndt, J. E., & H. Roberts, D. (2020). Bathymetry constrains ocean heat supply to Greenland's largest glacier tongue. *Nature Geoscience*, *13*.

Schaffer, J., von Appen, W.-J., Dodd, P. A., Hofstede, C., Mayer, C., de Steur, L., & Kanzow, T. (2017). Warm water pathways toward Nioghalvfjerdsfjorden glacier, Northeast Greenland. *Journal of Geophysical Research: Oceans*, *122*(5), 4004–4020. https://doi.org/10.1002/2016jc012462

Straneo, F., & Cenedese, C. (2015). The dynamics of Greenland's glacial Fjords and their role in climate. *Annual Review of Marine Science*, *7*(1), 89–112. https://doi.org/10.1146/annurev-marine-010213-135133

Straneo, F., & Heimbach, P. (2013). North Atlantic warming and the retreat of Greenland's outlet glaciers. *Nature*, *504*(7478), 36–43. https://doi.org/10.1038/nature12854

Straneo, F., Heimbach, P., Sergienko, O., Hamilton, G., Catania, G., Griffies, S., et al. (2013). Challenges to understanding the dynamic response of Greenland's marine terminating glaciers to oceanic and atmospheric forcing. *Bulletin of the American Meteorological Society*, *94*(8), 1131–1144. https://doi.org/10.1175/bams-d-12-00100.1

Talley, L. D., Pickard, G., Emery, W., & Swift, J. (2011). *Descriptive physical oceanography: An Introduction* (6th edn.). Boston, MA: Elsevier

Topp, R., & Johnson, M. (1997). Winter intensification and water mass evolution from yearlong current meters in the Northeast Water Polynya. *Journal of Marine Systems*, *10*(1). https://doi.org/10.1016/S0924-7963(96)00083-8

van den Broeke, M., Bamber, J., Ettema, J., Rignot, E., Schrama, E., van de Berg, W. J., et al. (2009). Partitioning recent Greenland mass loss. *Science*, *326*(5955), 984–986. https://doi.org/10.1126/science.1178176

von Appen, W.-J., Schauer, U., Hattermann, T., & Beszczynska-Möller, A. (2016). Seasonal cycle of mesoscale instability of the West Spitsbergen Current. *Journal of Physical Oceanography*, *46*(4), 1231–1254. https://doi.org/10.1175/jpo-d-15-0184.1

Washam, P., Nicholls, K. W., Münchow, A., & Padman, L. (2019). Summer surface melt thins petermann gletscher ice shelf by enhancing channelized basal melt. *Journal of Glaciology*, *65*(252), 662–674. https://doi.org/10.1017/jog.2019.43

Wilson, N. J., & Straneo, F. (2015). Water exchange between the continental shelf and the cavity beneath Nioghalvfjerdsbræ (79 North Glacier). *Geophysical Research Letters*, *42*(18), 7648–7654. https://doi.org/10.1002/2015gl064944

Wilson, N., Straneo, F., & Heimbach, P. (2017). Satellite-derived submarine melt rates and mass balance (2011–2015) for Greenland's largest remaining ice tongues. *The Cryosphere*, *11*(6), 2773–2782. https://doi.org/10.5194/tc-11-2773-2017